

The Current State of Reconstruction Technologies for 3D X-ray Microscopy including Algorithmic Innovation for AI-based Recovery

April 26, 10:00am - 11:00am EDT

Many properties can only be fully understood in 3D, such as porosity and tortuosity in porous materials, network connection maps in neuroscience, or mechanical properties in 3D additively manufactured structures. X-ray microscopy provides a unique method to image samples non-destructively in 3D across a wide range of materials and life sciences.

Watch this session during the WAS Virtual Conference:



Nicolas Guenichault, Ph.D.



Dr. Stephen T. Kelly, Ph.D.

Register Now

This talk is sponsored by



Spectroelectrochemical and Chemical Evidence of Surface Passivation at Zinc Ferrite (ZnFe_2O_4) Photoanodes for Solar Water Oxidation

Yongpeng Liu, Meng Xia, Liang Yao, Mounir Mensi, Dan Ren, Michael Grätzel, Kevin Sivula, and Néstor Guijarro*

Recent advances in low-cost manufacturing as well as in bulk/interface engineering have positioned zinc ferrite (ZnFe_2O_4 , ZFO) in the spotlight as a candidate material for solar water oxidation. However, the severe recombination at the reactive interface remains as the main source of the poor onset potential. Although catalytic overlayers have shown to override, at least partially, the surface recombination, passivating-only coatings are barely explored despite holding the key to specifically suppress the recombination. Here, a sub-nanometer Al_2O_3 layer is conformally deposited onto nanostructured ZFO, leading to a 100 mV shift in the onset potential reaching 0.80 V versus reversible hydrogen electrode (RHE) and a fourfold photocurrent increase at 1.0 V versus RHE. The passivation-only effect of Al_2O_3 is confirmed by the slowing down of the surface recombination detected by intensity-modulated photocurrent spectroscopy and by the transient photovoltage and photoluminescence experiments. Further characterization of the chemical states at the reactive interface reveals that the partial filling of the surface oxygen vacancies and the formation of a $\text{Zn}^{2+}\text{--Al}^{3+}$ Lewis adduct are potentially involved in the surface passivation. This study not only demonstrates that Al_2O_3 improves ZFO's onset potential but also sheds light on the up until now unknown surface passivation mechanism.

with an overall photovoltage (>1.23 V) to guarantee an economically-relevant H_2 production rate. Metal oxides have been long pursued as candidate materials for solar water oxidation (photoanode) given their earth-abundant composition, and specially, their durability under the harsh oxidative conditions associated with the O_2 evolution reaction.^[3–5] However, these materials are prone to a high degree of recombination at the reactive interface,^[6–9] which ultimately limits the photovoltage generated and hence, the photocurrent onset potential (V_{on}) obtained, therefore urgently demanding for new strategies to heal this interface. Indeed, several surface passivation routes, involving Ga_2O_3 ,^[10] Al_2O_3 ,^[11] SiO_2 ,^[12] and TiO_2 ^[13] coatings, have been so far described for well-established photoanode materials such as $\alpha\text{-Fe}_2\text{O}_3$ and BiVO_4 .


In recent years, spinel zinc ferrite (ZnFe_2O_4 , ZFO) has gained prominence among the emergent candidate materials for solar water splitting, owing to, for instance, its suitable band gap ($E_g \approx 2$ eV),

low-cost processing and potential for further adjusting the electronic properties by tuning cation disorder within the lattice.^[14–16] Advances in the performance of ZFO have primarily originated from fine-tuning the bulk electronic properties. For instance, Lee and co-workers demonstrated that introducing oxygen vacancies,^[17,18] Sn^{4+} or Ti^{4+} improved the performance by increasing the doping density,^[19] while showing a circumstantial contribution to the surface passivation. Likewise, Zhu et al. showed that modulating the inversion degree in this material allowed to adjust the bulk transport properties reaching a record-value photocurrent.^[20] Interestingly, the authors noticed that the higher the synthesis temperature the smoother surface (less-defective) and the lower the surface recombination, with V_{on} improving from 1.2 to 0.9 V versus reversible hydrogen electrode (RHE). Obviously, most of these reports incorporate a cocatalyst to improve the kinetics of water oxidation which, in turn, alleviate the surface recombination. However, few reports have attempted to selectively passivate the ZFO's surface with non-catalytic overlayers. Ma et al. reported that coating ZFO with SiO_2 improved the photocurrent from 0.15 to 0.21 mA cm^{-2}

1. Introduction

Solar water splitting by means of photoelectrochemical (PEC) tandem cells is one of the most appealing technologies for the production of green hydrogen, given their competitive theoretical conversion efficiency ($>20\%$) together with the simple top- and bottom-cell architecture that simplifies upscaling.^[1,2] Here, two semiconductor materials work in a concerted way harvesting the sunlight, and generating a photocurrent together

Y. Liu, M. Xia, Dr. L. Yao, Dr. M. Mensi, Dr. D. Ren, Prof. M. Grätzel, Prof. K. Sivula, Dr. N. Guijarro^[†]
Institute of Chemical Sciences and Engineering
École Polytechnique Fédérale de Lausanne (EPFL)
Station 6, Lausanne 1015, Switzerland
E-mail: nestor.guijarro@epfl.ch

 The ORCID identification number(s) for the author(s) of this article can be found under <https://doi.org/10.1002/adfm.202010081>.

^[†]Present address: Institute of Electrochemistry, Universidad de Alicante, Apartat 99, E-03080 Alacant, Spain

DOI: 10.1002/adfm.202010081

at 1.23 V versus RHE, while V_{on} remained unchanged.^[21] Similarly, Sahu et al. detected an improved photocurrent but an unaltered V_{on} upon coating ZFO with Al_2O_3 .^[22] However, the numerous uncontrollable factors (e.g., surface coverage and thickness) in the chemical bath deposition (CBD) of Al_2O_3 poses severe difficulties to elucidate the effect of this overlayer. There is, therefore, a lack of strategies to specifically suppress the surface recombination as well as of understanding on how the passivation mechanism operates.

In this study, we report for the first time on the passivating effect of a sub-nanometer Al_2O_3 thin film deposited onto ZFO, evidenced by ≈ 100 mV shift of V_{on} . We found that this coating not only slowed down the surface recombination, but also enhanced the built-in electric field, reinforcing its passivating role. Detailed characterization of the chemical states at reactive interface provided compelling evidence that the passivation mechanism involves both the partial refilling of the oxygen vacancies and the formation of a $Zn^{2+}-Al^{3+}$ Lewis adduct at the ZFO/ Al_2O_3 interface.

2. Results and Discussion

Figure 1 shows the linear sweep voltammetry under chopped-light illumination recorded for bare ZFO. At first sight, the

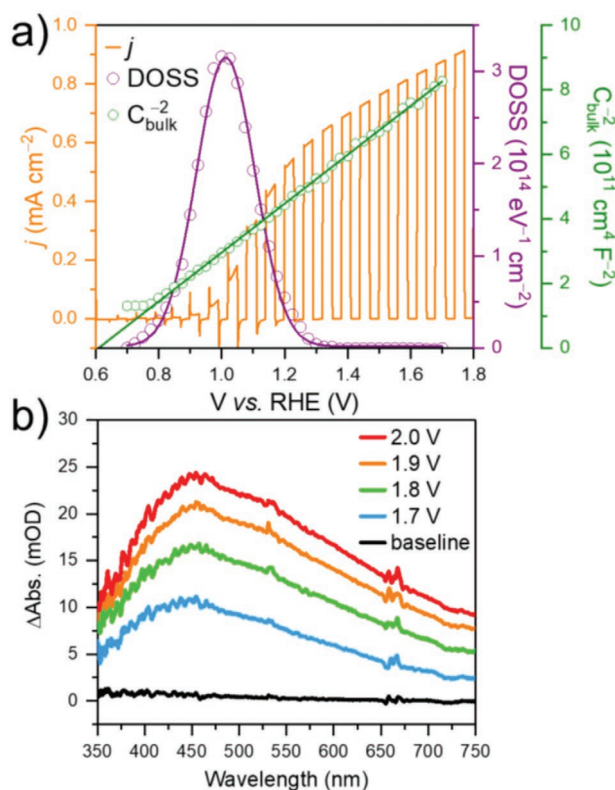


Figure 1. a) Linear sweep voltammetry of ZFO recorded under intermittent illumination (orange line), Mott-Schottky plot (green circles) and corresponding fitting (green line), as well as the density of surface states (DOSS, purple circles) including the corresponding Gaussian fit (purple line). b) Operando UV-vis spectra recorded under different applied potential in the absence of external illumination.

0.9 V versus RHE V_{on} resembles those reported previously in literature,^[23] whereas the 0.56 mA cm⁻² photocurrent density at 1.23 V versus RHE is amongst the highest reported for cocatalyst-free ZFO photoanodes.^[18–22] It is worth noting that the saturation photocurrent is mostly limited by the short hole diffusion length (≈ 3 nm, see Supporting Information for details) as it is commonplace among ferrites.^[24] Note that the transient photocurrent (TPC) spikes detected in the voltage range spanning from 0.6 to 1.2 V versus RHE provide evidence of the surface recombination.^[25,26] To assess the degree and origin of the voltage losses occurring under operation, EIS experiments were performed both in dark and light conditions. Details on the electrical models and equations employed in the EIS data analysis can be found in the Supporting Information. Mott-Schottky (MS) plot revealed that the flat band potential is located at 0.6 V versus RHE, that is, 300 mV earlier than V_{on} (Figure 1). This late onset correlates well with the existence of surface recombination.^[27]

Further analysis of EIS data allowed to extract the density of surface states (DOSS), a proxy for the accumulated charge at the electrolyte interface under illumination, which is known to be linked to the surface recombination phenomena (Figure 1).^[24,28] DOSS seemingly extends from 0.5 to 1.3 V versus RHE. It must be, however, borne in mind that the splitting of the quasi-Fermi levels at ZFO's surface should be added if the actual position of the DOSS needs to be estimated. It is commonly accepted that the surface accumulated charge detected nearby the photocurrent onset corresponds to highly-oxidized intermediate species involved in the water oxidation reaction, although it cannot be discarded the participation of surface-trapped holes in the signal of DOSS.^[28–30] Either way, the buildup of holes at the interface will promote the surface recombination phenomena with photogenerated electrons.

To cast some light into the identity of the DOSS, operando UV-vis spectroscopy measurements were performed as a function of the applied potential, both in the absence and presence of an external bias light. Under monochromatic bias illumination (405 nm), a broad absorption band extending from 450 up to ≈ 760 nm and whose intensity exhibits a direct correlation with the applied potential was detected (Figure S8, Supporting Information). Similar optical signatures have been previously reported for other metal oxide (e.g., α -Fe₂O₃,^[31–33] IrO_x,^[34] and MnO_x^[35]) and concluded to be related primarily to reaction intermediates at the electrodes' surface. These experiments were repeated in the absence of external illumination to access a wider spectral range, since a longpass filter was used to protect the detector against the bias light. Figure 1b shows the operando UV-vis spectra recorded in the absence of bias light, exhibiting a broad band spanning from 350 to 750 nm and centered at around 455 nm. Note that higher applied potentials were required to trigger the water oxidation reaction and detect the buildup of surface holes given the lack of the energy input provided by light. It is worth highlighting that this optical signature is similar to that attributed to high-valent iron reaction intermediates ($-Fe^{IV} = O$) in α -Fe₂O₃ photoanodes located at around 580 nm,^[31,36] although it appears to blueshift in ZFO, as it has been previously shown for CuFe₂O₄.^[24] Note that similar studies performed on MnO₂ electrocatalysts under OER conditions revealed that the corresponding d-d transition

shifted toward lower wavelengths, when the high-valent Mn center was coordinated to electron-donating species, and in the opposite direction when the center was coordinated to electron-accepting species.^[37] Bearing in mind that iron adopts an octahedral coordination geometry in both Fe₂O₃ and ZFO, that is, each iron is connected to six oxygen ligands, it is not unreasonable to propose that changes in the chemical environment of high-valent iron centers could be responsible for the shift in the d–d transition. We hypothesize that given the reduced electronegativity of Zn compared to Fe, the oxygen ligands that are connected to Zn will exhibit a higher electron density and therefore, act as electron-donating ligands for the nearby high-valent Fe species. This could account for the changes in the ligand field splitting of the high-valent iron species that result in the observed shift in the d–d transition.

The DOSS was next fit to a Gaussian function, leading to an estimate total DOSS (N_{SS}) of $7.2 \times 10^{13} \text{ cm}^{-2}$. Note that this value is above the threshold considered to cause Fermi level pinning (FLP).^[38] In other words, FLP is expected to occur in the potential region wherein DOSS are detected. Since FLP is known to retard the development of band bending, it will limit the surface hole concentration, and thus, the surface potential that drives the water oxidation reaction which accounts for the late V_{on} of bare ZFO (see more details in Figure S9, Supporting Information). Note that catalytic overlayers have shown to shift V_{on} earlier owing to the reduced surface overpotential demanded for the oxygen evolution reaction, rather than by altering the FLP.^[39]

With the aim of suppressing the surface recombination and hence, tackle the late V_{on} , a sub-nanometer Al₂O₃ thin film was deposited onto ZFO. Angle-resolved X-ray photoelectron spectroscopy (ARXPS) confirmed the conformal distribution of Al₂O₃ over nanostructured ZFO (see Supporting Information for details). Figure 2a shows the linear sweep voltammetry recorded under illumination for bare and Al₂O₃-coated ZFO, as well as the DOSS. Surprisingly, the incorporation of Al₂O₃ triggers a 100 mV earlier V_{on} , that is, from 900 to 800 mV versus RHE, thus leading to a fourfold enhancement of the photocurrent at 1.0 V versus RHE albeit both photocurrent profiles virtually overlap from 1.4 V onward. Note that Sahu et al. did not detect any change in V_{on} after coating ZFO with Al₂O₃ deposited by CBD.^[22] Likely, the incomplete surface

coverage obtained by CBD could reduce the effectiveness of the passivation effect.^[40] EIS analyses were performed to find out the mechanisms whereby Al₂O₃ improves ZFO's performance. First, MS plot demonstrated that the flat band potential barely changed with the incorporation of Al₂O₃ (Figure S6, Supporting Information), therefore discarding a shift of the electronic bands induced by the overlayer, which could account for the earlier V_{on} .^[41] Second, N_{SS} decreased by 26% down to $5.3 \times 10^{13} \text{ cm}^{-2}$, which evidences a partial suppression of the FLP. Broadly speaking, the incorporation of Al₂O₃ caused the surface accumulated charge to drop which certainly contributed to mitigate the surface recombination. Note that the reduced N_{SS} could originate from either a decrease of the surface traps or an accelerated water oxidation reaction.

Intensity-modulated photocurrent spectroscopy (IMPS) was next implemented to decode the surface carrier dynamics, and estimate the changes that the rate constants for charge transfer (k_{tran}) and surface recombination (k_{rec}) suffer with the incorporation of Al₂O₃. Figures S10–S12, Supporting Information display the Nyquist plots associated to the IMPS response for both bare and Al₂O₃-coated ZFO at different applied bias as well as the characteristic high- and low-frequency intersects (HFI and LFI, respectively) with the real axis. It is generally accepted that the HFI is directly proportional to the flux of holes arriving at the electrolyte interface, whereas LFI correlates with the flux of holes transferred to the electrolyte.^[42] First, the HFI increased slightly upon Al₂O₃ deposition especially in the 0.9–1.4 V versus RHE range suggesting that the band bending that drives holes toward the surface got strengthened with the coating (Figure S9, Supporting Information). Second, the LFI showed a much drastic increase with Al₂O₃ in the same voltage range, supporting the notion that this overlayer suppressed the surface recombination. Both results hint at the role of the Al₂O₃ overlayer as FLP mitigator. Decoupling both k_{tran} and k_{rec} by fitting the Nyquist plot will further clarify the effects of Al₂O₃. As shown in Figure 2b, k_{rec} decreases with increasing applied bias. This is not unexpected, since the increase of the band bending will slow down the recombination.^[25] Interestingly, Al₂O₃ caused k_{rec} to drop in all the voltage range and steepened the change of k_{rec} with the applied potential. The former result is commonly attributed the passivation of surface traps,^[10] whereas the latter evidences the suppression of the FLP and

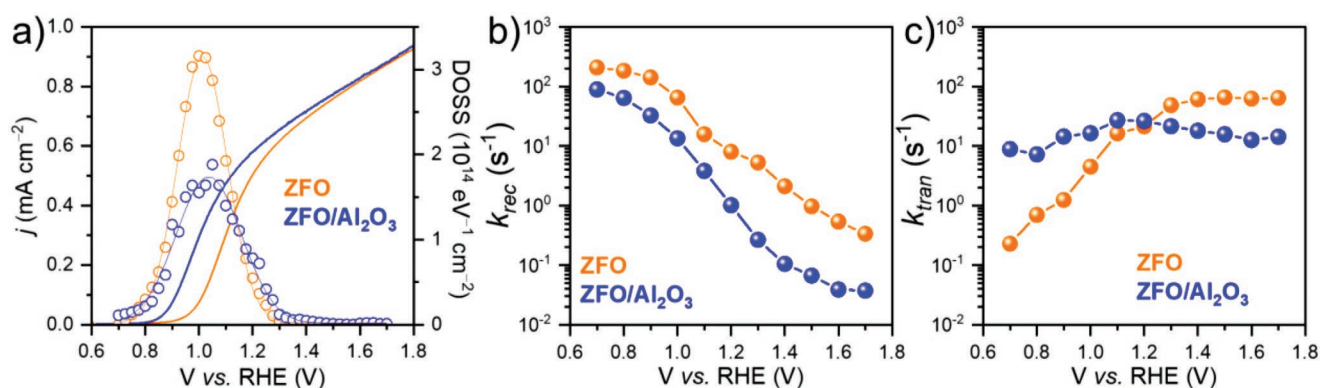


Figure 2. Comparison between the PEC of ZFO (orange) and ZFO/Al₂O₃ (blue). a) Linear sweep voltammetry under constant illumination and DOSS. b) Surface recombination and c) charge transfer rate constants as a function of the applied potential.

the concomitant reinforcement of the built-in electric field. The behavior of k_{tran} appears as well to be drastically affected by the presence of Al_2O_3 (Figure 2c). In the absence of Al_2O_3 k_{tran} increases with the applied potential until reaching 1.3 V versus RHE, whereas in the presence, k_{tran} remains virtually constant in all the range. Since the FLP is known to cause k_{tran} to change with the applied bias,^[6,25] these results further support the notion that Al_2O_3 passivates ZFO's surface. It is worth noting that k_{tran} increases with Al_2O_3 , particularly at low applied bias, wherein the passivation could lead to a comparatively more oxidizing surface potential. Finally, the charge transfer efficiency (TE), a proxy for the kinetic dominance of k_{tran} over k_{rec} was calculated demonstrating that the incorporation of Al_2O_3 shifts the quantitative surface charge transfer (TE = 100%) 300 mV earlier, from 1.6 to 1.3 V versus RHE (Figure S13, Supporting Information).

With the impact of Al_2O_3 at the surface-related carrier dynamics set in place, we next evaluated the influence of this overlayer on the electron collection at the rear contact. Figure 3a displays the TPC experiment performed for bare and Al_2O_3 -coated ZFO under short circuit conditions. Note that the illumination was carried out from the electrolyte side to deliberately induce the carrier photogeneration far from the substrate. Interestingly, the incorporation of Al_2O_3 triggers a faster electron collection, as evidenced by the decreased electron transient time (τ_t) from 1.74 to 0.45 ms. We hypothesize that the shorter τ_t could arise from the stronger built-in electric field achievable in the presence of Al_2O_3 , which could more effectively swept the electrons toward the rear contact. Note that τ_t and the film thickness can be used to define an apparent electron diffusion coefficient (D_e) that increases from 2.4×10^{-7} to $9.3 \times 10^{-7} \text{ cm}^2 \text{ s}^{-1}$ with Al_2O_3 (see Supporting Information for details).

Open circuit measurements were undertaken to further confirm the suppression of surface-trap states. First, transient

photovoltage (TPV) experiments revealed a slower decay in the presence of Al_2O_3 (Figure 3b), with the characteristic electron recombination lifetime (τ_r) increasing from 36 to 61 ms. The lengthening of τ_r provide further evidence of the reduced density of recombination centers in the system.^[26] Second, the steady-state photoluminescence (PL) spectrum of ZFO showed to increase in magnitude upon Al_2O_3 coating (Figure 3c). This supports the notion that the overlayer effectively passivates surface traps involved in the non-radiative recombination pathways. It is worth noting that the PL extends over a rather broad range, that is, from 500 to $\approx 700 \text{ nm}$, which appears to result from various emission centers simultaneously active. To better identify and monitor the different emission centers, PL spectra were accurately fit using three Gaussian curves centered at 534, 577, and 630 nm, respectively (Figure S16, Supporting Information). The lower-wavelength band could be assigned to the band edge recombination, since it is located nearby the onset of light absorption (Figure S15a, Supporting Information), whereas the longer-wavelength signatures could be assigned to recombination processes involving mid-gap states. Indeed, it is well-known that the presence of oxygen vacancies cause the appearance of trap states that lie inside the band gap which are actively involved in the emission characteristics of ZFO and related oxides.^[43,44] Note that commonly oxygen vacancies are artificially induced in ZFO to improve the electron doping density.^[18,20] In addition, the PL deactivation kinetics were further assessed by monitoring the PL decay at 575 nm. Time-resolved PL (TRPL) evidenced an increased lifespan of the PL in the presence of Al_2O_3 , with the characteristic time constant (τ) rising from 9.0 to 12.4 μs , which further supports the effective passivation of surface traps involved in non-radiative PL deactivation pathways.

With the electronic effects of the Al_2O_3 in hand, we next attempted to unveil the chemical changes linked to the passivation mechanism. To do so the chemical states of ZFO interface were characterized by XPS. Figure S18, Supporting Information displays the high-resolution XPS spectra of Fe, O, Zn, and Al, collected from bare and Al_2O_3 -coated ZFO samples. First, the Fe 2p spectra did not exhibit noticeable changes with the incorporation of Al_2O_3 (see Supporting Information for details), suggesting that the electron density surrounding Fe centers was not altered with the coating. Second, the O 1s spectra display asymmetric bands with multiple contributions, corresponding to, for instance, oxygen ions in regular sites of the lattice or in low-coordinated sites, or adsorbed species such as hydroxyl ions or contaminants (see Supporting Information for details). Careful analysis of the data affords to estimate changes in the surface oxygen defects, which appear to decrease with the Al_2O_3 deposition. This is not unexpected since the ALD deposition could refill those surface oxygen vacancies. It is, however, important to note that although bulk oxygen defects are beneficial to improve the electron density of the material, excess of surface oxygen vacancies are known to be detrimental for the performance since they induce mid-gap states that promote surface recombination.^[18] Third, Zn LMM spectrum (Figure 4a), unlike Zn 2p signal (Figure S18, Supporting Information), appears to be significantly altered by the Al_2O_3 , likely because of the greater sensitivity of the Zn LMM Auger peak to changes in the chemical state of Zn. Qualitatively, the appearance of a

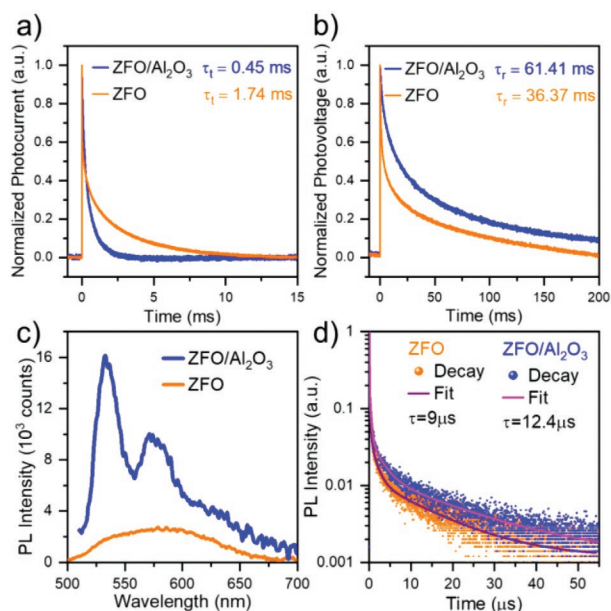


Figure 3. Comparison of bulk charge transport/recombination properties between ZFO (orange) and ZFO/ Al_2O_3 (blue). a) TPC and b) TPV spectra. c) Steady-state photoluminescence and d) TRPL spectra.

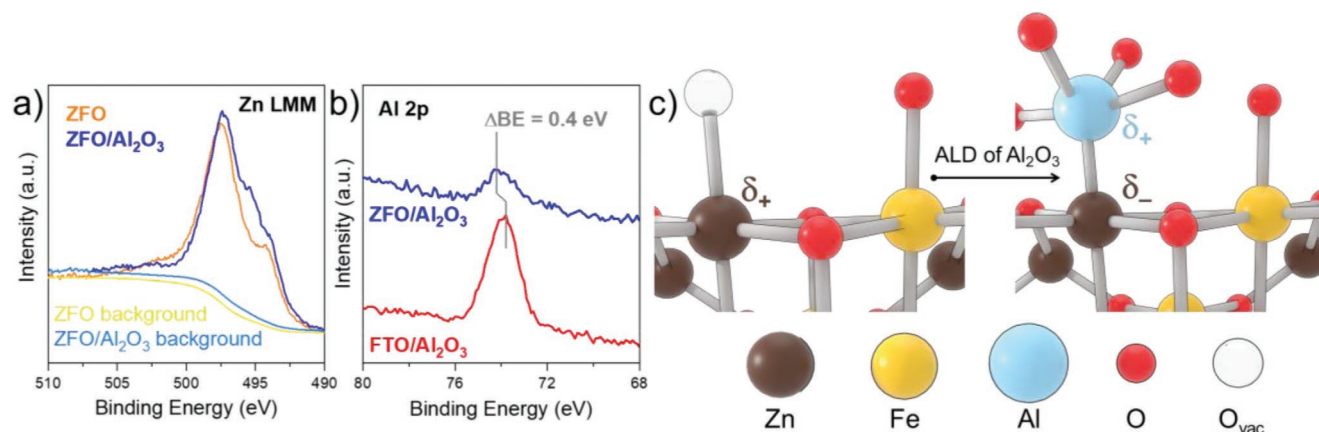


Figure 4. XPS analysis on ZFO (orange), ZFO/Al₂O₃ (blue), and reference FTO/Al₂O₃ (red). a) Zn LMM spectra. b) Al 2p spectra. c) Illustration of the formation of Zn²⁺–Al³⁺ Lewis adduct.

shoulder centered at around 495.3 eV suggests an increased electron density in the surroundings of surface Zn ions upon Al₂O₃ deposition. Interestingly, the analysis of the binding energy of the Al 2p peak on ZFO reveals a 0.4 eV upward shift with respect a reference Al₂O₃ thin film (Figure 4b), which indicates a relative decrease in the electron density surrounding Al ions when interfaced with ZFO. These results support the formation of a Zn²⁺–Al³⁺ Lewis adduct wherein Al donates electron density toward the Zn center. Overall, the analyses of the chemical states at the interface suggest that unsaturated Zn centers are more plausibly the recombination centers passivated by Al₂O₃. The Al ion refills the oxygen vacancy site while increasing the electron density around the Zn site to overcompensate for the electron-deficit induced by the oxygen defect.

3. Conclusion

In this study, we addressed the commonplace low V_{on} exhibited by non-catalyst-coated ZFO photoanodes by taking advantage, for the first time, of a sub-nanometer-thick Al₂O₃ overlayer and by deciphering its beneficial impact on the PEC response. Coating with Al₂O₃ demonstrated to shift V_{on} 100 mV earlier, up to 0.8 V versus RHE, while the photocurrent exhibits a four-fold enhancement at 1.0 V versus RHE. EIS and IMPS analyses revealed that Al₂O₃ mainly operates by suppressing the FLP encountered at low applied potential, as confirmed by the slowing down of the surface recombination and strengthening of the band bending. Open circuit potential measurements, such as TPV and PL, further corroborated the elimination of surface recombination center with Al₂O₃ displaying a longer lifespan of the photogenerated carriers. Finally, a detailed characterization of the chemical states at ZFO's interface shed some light on the so far unknown chemical mechanism behind the passivation phenomena. We found that Al₂O₃ primarily refills surface oxygen vacancies while forming a Zn²⁺–Al³⁺ Lewis adduct at the interface. Overall, these results not only demonstrated that Al₂O₃ passivates ZFO's surface and improves V_{on} , but also identified unsaturated Zn sites as the most plausible recombination centers tackled by Al₂O₃. In a more general vein, our findings established and rationalize a new strategy

to specifically heal ZFO's surface recombination, which we are convinced will lead further optimization of ZFO's and other emerging metal oxides' performance.

4. Experimental Section

Materials: ZFO thin films were synthesized as reported elsewhere.^[20] First, F:SnO₂ (FTO) coated glass substrates (Solaronix TCO10-10, 8 Ω sq^{−1}) were positioned vertically in an aqueous solution 0.15 M iron chloride hexahydrate (FeCl₃·6H₂O, 99+%, Acros) and 1 M sodium nitrate (NaNO₃, 99+%, Acros). A precursor film of β-FeOOH nanorods were grown hydrothermally on FTO at 100 °C for 3 h in a universal oven (Mettler UF 30 plus). After rinsing with deionized water (18.2 MΩ·cm, Synergy) and drying with compressed air, these β-FeOOH thin films were placed in a pre-heated hot plate (VWR 10027-246) at 100 °C to drop-cast an excess of 0.1 M zinc nitrate hexahydrate (Zn(NO₃)₂·6H₂O, 98%, abcr) aqueous solution. Second, these zinc nitrate coated β-FeOOH thin films were introduced into a tube furnace (MTI OTF-1200X-S) preheated at 600 °C for 20 min followed by natural cooling to form spinel type ZFO. Third, these as-prepared thin films were soaked in 5 M NaOH (Reactolab SA) for 4 h to etch away ZnO crust at surface. Finally, a 60 min hydrogenation procedure at 200 °C was performed. Morphological characterization, X-ray diffraction, Raman spectrum and UV–vis spectrum can be found in Figures S1–S3, S15, Supporting Information.

Al₂O₃ overlayer was deposited on ZFO by atomic layer deposition (ALD) using a thermal ALD system (Savannah 100, Cambridge NanoTech). The substrate was heated to 150 °C in a vacuum chamber. Trimethylaluminum (TMA, Sigma Aldrich) was used as aluminum precursor and deionized water was used as oxygen precursor. TMA was introduced into the vacuum chamber under a nitrogen flow of 5 sccm. The deposition procedure consisted 0.2 s pulse time for both precursors and each followed by a 15 s nitrogen pumping time. The growth rate of Al₂O₃, that was previously determined by ellipsometry,^[11] was 0.15 nm per cycle. All the ZFO/Al₂O₃ thin films reported in this manuscript were prepared using 3 cycles of Al₂O₃ (≈0.45 nm). The conformal coating of Al₂O₃ was confirmed by XPS and ARXPS, see Figure S19, Supporting Information. The reference Al₂O₃ thin film utilized for comparison with the sub-nanometer-thick Al₂O₃ coating on ZFO was prepared directly on FTO by using 200 ALD cycles (≈30 nm thickness).

Photoelectrochemical Characterization: A Cappuccino-type electrochemical cell using the ZFO photoanode as working electrode (aperture area 0.238 cm²), a platinum wire counter electrode, and silver chloride reference electrode (Ag/AgCl/Sat. KCl, ALS RE-1CP) was used for all electrochemical tests. The 3-electrode configuration was connected to a computer-controlled Bio-Logic SP-300 potentiostat. An array of white

LED (Cree XLamp MC-E Color) with a calibrated incident photon flux of $9.25 \times 10^{20} \text{ m}^{-2} \text{ s}^{-1}$ (≈ 0.66 sun in terms of photon flux and spectral irradiance, see Figure S20, Supporting Information for irradiation spectrum comparison) was used for consistency as light source in all the experiments, namely, linear sweep voltammetry measurements, PEC impedance, and IMPS/IMVS tests. Unless stated otherwise, ZFO working electrode was illuminated from the substrate-side in 1 M NaOH electrolyte (pH 13.6, Reactolab SA). For sacrificial agent oxidation experiments, 0.5 mL of hydrogen peroxide (H_2O_2 , 30%, Reactolab SA) was added into 9.5 mL of 1 M NaOH solution. A 20 mV s^{-1} scan rate was set for linear sweep voltammetry. For impedance measurements, a 25 mV sinusoidal voltage perturbation was applied with the frequency range of 1 MHz to 0.1 Hz. The impedance response was corrected for a surface roughness factor of 18 (see Figure S4, Supporting Information for roughness factor determination) and it was fit using an equivalent circuit modeling software ZView (Scribner Associates). An array of RGBW Star LEDs (Cree) with a calibrated incident photon flux of $1.01 \times 10^{21} \text{ m}^{-2} \text{ s}^{-1}$ was used to provide electrolyte-side monochromatic (452 nm) illumination. All the measurement potentials were converted into the RHE by the Nernst equation.

For IMPS/IMVS measurements, the light intensity was controlled by supplying a 600 mA DC background current and was additionally modulated by an arbitrary function generator (Tektronix AFG3021C) with a 60 mA sinusoidal amplitude ($\approx 10\%$ modulation depth) ranged from 10 kHz to 0.1 Hz. In IMPS experiments, a Thompson Electrochem potentiostat (model 251) was used to control the applied potential while the photocurrent response was monitored by a digital phosphor oscilloscope (Tektronix DPO7254C) through a 50Ω series resistor (Velleman E6/E12) with the counter electrode. In IMVS experiments, the open-circuit voltage response was recorded by the oscilloscope via a BNC to banana adapter (Pomona Electronics). IMPS data were processed and fitted using a custom Python program with Imfit package to perform curve fitting with nonlinear regression.

Operando UV-vis spectroscopy: A cuvette (Hellma Analytics OS, 10 mm) coupled with a 3D printed cuvette electrochemical extender were used to set up a 3-electrode configuration containing a $9 \times 50 \text{ mm}$ ZFO working electrode, a mini Ag/AgCl reference electrode (ALS RE-1S), and a platinum wire counter electrode. The 3-electrode setup was connected to a Bio-Logic SP-50 potentiostat and was placed inside a UV-vis spectrophotometer (Shimadzu UV-3600). External illumination was provided by a 405 nm laser diode (Thorlabs L405P150) running at 66.7 mW. A 450 nm longpass filter (Thorlabs FEL0450) was positioned in front of the UV-vis detector to prevent light saturation due to laser diode. Illustration of experimental setup can be found in Figure S7, Supporting Information.

Transient Photocurrent/Photovoltage Spectroscopy: TPC spectroscopy was carried out in a 2-electrode configuration with a ZFO (or ZFO/ Al_2O_3) working electrode and a Pt mesh counter electrode in a Cappuccino-type electrochemical cell. The 2-electrode system was connected to a 50Ω series resistor (Velleman E6/E12) which was probed by a digital phosphor oscilloscope (Tektronix DPO7254C) through a differential probe (Tektronix TDP3500). In TPV spectroscopy the differential probe was directly connected to working electrode and reference electrode under open circuit condition. Both TPC and TPV signals were recorded by the oscilloscope on averaging acquisition mode with more than 1000 samples. Note that the electron transient time (τ_t) and electron recombination lifetime (τ_r) were the average time constant estimate from the exponential fit of the decays. In both TPC and TPV measurements, working electrode was front illuminated by a high energy broadly tunable diode-pumped solid-state Nd:YAG laser system (EKSPLA, NT230-50-SF-2H, pulse duration 3–6 ns) at 410 nm wavelength with a power of 1.11 mJ cm^{-2} . A biased Si detector (Thorlabs, DET36A/M) was used to trigger the oscilloscope. The entire TPC/TPV setup was enclosed with blackout and laser safety materials (Thorlabs).

Steady-State and Time-Resolved Photoluminescence Spectroscopy: Steady-state PL spectra were recorded on a high resolution PL spectrofluorometer (Horiba Jobin Yvon Fluorolog-3). In TRPL spectroscopy measurement, a nanosecond LED with 390 nm peak

wavelength (Horiba NanoLED N-390, pulse width $< 1.3 \text{ ns}$) was used to excite sample. TRPL decay was tracked at 575 nm.

Supporting Information

Supporting Information is available from the Wiley Online Library or from the author.

Acknowledgements

This work was supported by the Swiss National Science Foundation (SNSF) under the Ambizione Energy grant (PZENP2_166871) and Strategic Japanese-Swiss Science and Technology grant (No. 514259). M.X. is grateful for the support from the China Scholarship Council (No. CSC201806160172). Dr. Florian Le Formal and Mr. Harald Holze are gratefully acknowledged for the light modulation setup. Dr. Florent Boudoire is gratefully acknowledged for fitting IMPS data.

Conflict of Interest

The authors declare no conflict of interest.

Data Availability Statement

Research data are not shared.

Keywords

intensity-modulated photocurrent spectroscopy, Lewis adduct, surface passivation, water splitting, ZnFe_2O_4

Received: November 23, 2020

Revised: January 5, 2021

Published online: February 15, 2021

- [1] J. Lin, W. Wang, G. Li, *Adv. Funct. Mater.* **2020**, *30*, 2005677.
- [2] Y. Wang, W. Tian, C. Chen, W. Xu, L. Li, *Adv. Funct. Mater.* **2019**, *29*, 1809036.
- [3] A. Kormányos, E. Kecsenovity, A. Honarfar, T. Pullerits, C. Janáky, *Adv. Funct. Mater.* **2020**, *30*, 2002124.
- [4] Y. Zhang, Y. Li, D. Ni, Z. Chen, X. Wang, Y. Bu, J.-P. Ao, *Adv. Funct. Mater.* **2019**, *29*, 1902101.
- [5] Y. Liu, J. Quiñero, L. Yao, X. D. C. Pereira, M. Mensi, R. Gómez, K. Sivula, N. Guijarro, *J. Mater. Chem. A* **2021**, *9*, <https://doi.org/10.1039/D0TA11541J>.
- [6] C. Zachäus, F. F. Abdi, L. M. Peter, R. van de Krol, *Chem. Sci.* **2017**, *8*, 3712.
- [7] Y. Yang, S. Niu, D. Han, T. Liu, G. Wang, Y. Li, *Adv. Energy Mater.* **2017**, *7*, 1700555.
- [8] D. K. Zhong, S. Choi, D. R. Gamelin, *J. Am. Chem. Soc.* **2011**, *133*, 18370.
- [9] C. Xing, Y. Liu, Y. Zhang, X. Wang, P. Guardia, L. Yao, X. Han, T. Zhang, J. Arbiol, L. Soler, Y. Chen, K. Sivula, N. Guijarro, A. Cabot, J. Llorca, *ACS Appl. Mater. Interfaces* **2021**, *13*, 449.
- [10] J. E. Thorne, J.-W. Jang, E. Y. Liu, D. Wang, *Chem. Sci.* **2016**, *7*, 3347.
- [11] F. Le Formal, N. Tétreault, M. Cornuz, T. Moehl, M. Grätzel, K. Sivula, *Chem. Sci.* **2011**, *2*, 737.
- [12] L. Steier, I. Herraiz-Cardona, S. Gimenez, F. Fabregat-Santiago, J. Bisquert, S. D. Tilley, M. Grätzel, *Adv. Funct. Mater.* **2014**, *24*, 7681.

- [13] J. Gu, Q. Huang, Y. Yuan, K.-H. Ye, Z. Wang, W. Mai, *J. Mater. Chem. A* **2017**, 5, 20195.
- [14] A. G. Hufnagel, K. Peters, A. Müller, C. Scheu, D. Fattakhova-Rohlfing, T. Bein, *Adv. Funct. Mater.* **2016**, 26, 4435.
- [15] J. H. Kim, J. H. Kim, J.-W. Jang, J. Y. Kim, S. H. Choi, G. Magesh, J. Lee, J. S. Lee, *Adv. Energy Mater.* **2015**, 5, 1401933.
- [16] J. H. Kim, Y. J. Jang, S. H. Choi, B. J. Lee, M. H. Lee, J. S. Lee, *ACS Sustainable Chem. Eng.* **2019**, 7, 944.
- [17] J. H. Kim, Y. J. Jang, S. H. Choi, B. J. Lee, J. H. Kim, Y. B. Park, C.-M. Nam, H. G. Kim, J. S. Lee, *J. Mater. Chem. A* **2018**, 6, 12693.
- [18] J. H. Kim, Y. J. Jang, J. H. Kim, J.-W. Jang, S. H. Choi, J. S. Lee, *Nanoscale* **2015**, 7, 19144.
- [19] J. H. Kim, J. H. Kim, J. H. Kim, Y. K. Kim, J. S. Lee, *Sol. RRL* **2020**, 4, 1900328.
- [20] X. Zhu, N. Guijarro, Y. Liu, P. Schouwink, R. A. Wells, F. L. Formal, S. Sun, C. Gao, K. Sivula, *Adv. Mater.* **2018**, 30, 1801612.
- [21] H. Ma, M. A. Mahadik, S. R. Kim, M. Wang, H. I. Ryu, H. S. Chung, W. S. Chae, H. Park, J. S. Jang, *J. Taiwan Inst. Chem. Eng.* **2020**, 107, 89.
- [22] T. K. Sahu, A. K. Shah, G. Gogoi, A. S. Patra, M. S. Ansari, M. Qureshi, *Chem. Commun.* **2018**, 54, 10483.
- [23] Von is defined as the potential where the photocurrent density equals $10 \mu\text{A cm}^{-2}$.
- [24] Y. Liu, F. L. Formal, F. Boudoire, L. Yao, K. Sivula, N. Guijarro, *J. Mater. Chem. A* **2019**, 7, 1669.
- [25] L. M. Peter, K. G. U. Wijayantha, A. A. Tahir, *Faraday Discuss.* **2012**, 155, 309.
- [26] F. Le Formal, K. Sivula, M. Grätzel, *J. Phys. Chem. C* **2012**, 116, 26707.
- [27] J. F. McCann, J. Pezy, *J. Electrochem. Soc.* **1981**, 128, 1735.
- [28] B. Klahr, S. Gimenez, F. Fabregat-Santiago, T. Hamann, J. Bisquert, *J. Am. Chem. Soc.* **2012**, 134, 4294.
- [29] Y. Liu, N. Guijarro, K. Sivula, *Helv. Chim. Acta* **2020**, 103, e2000064.
- [30] O. Zandi, T. W. Hamann, *Nat. Chem.* **2016**, 8, 778.
- [31] B. Klahr, T. Hamann, *J. Phys. Chem. C* **2014**, 118, 10393.
- [32] T. Takashima, K. Ishikawa, H. Irie, *J. Phys. Chem. C* **2016**, 120, 24827.
- [33] Y. Liu, F. Le Formal, F. Boudoire, N. Guijarro, *ACS Appl. Energy Mater.* **2019**, 2, 6825.
- [34] H. Ooka, Y. Wang, A. Yamaguchi, M. Hatakeyama, S. Nakamura, K. Hashimoto, R. Nakamura, *Phys. Chem. Chem. Phys.* **2016**, 18, 15199.
- [35] T. Takashima, K. Hashimoto, R. Nakamura, *J. Am. Chem. Soc.* **2012**, 134, 1519.
- [36] M. Barroso, C. A. Mesa, S. R. Pendlebury, A. J. Cowan, T. Hisatomi, K. Sivula, M. Grätzel, D. R. Klug, J. R. Durrant, *Proc. Natl. Acad. Sci. USA* **2012**, 109, 15640.
- [37] T. Takashima, A. Yamaguchi, K. Hashimoto, H. Irie, R. Nakamura, *Electrochemistry* **2014**, 82, 325.
- [38] A. J. Bard, A. B. Bocarsly, F. R. F. Fan, E. G. Walton, M. S. Wrighton, *J. Am. Chem. Soc.* **1980**, 102, 3671.
- [39] B. Klahr, S. Gimenez, F. Fabregat-Santiago, J. Bisquert, T. W. Hamann, *J. Am. Chem. Soc.* **2012**, 134, 16693.
- [40] Z. Fan, Z. Xu, S. Yan, Z. Zou, *J. Mater. Chem. A* **2017**, 5, 8402.
- [41] R. Wick-Joliat, T. Musso, R. R. Prabhakar, J. Löckinger, S. Siol, W. Cui, L. Sévery, T. Moehl, J. Suh, J. Hutter, M. Iannuzzi, S. D. Tilley, *Energy Environ. Sci.* **2019**, 12, 1901.
- [42] A. Tsyganok, D. Klotz, K. D. Malviya, A. Rothschild, D. A. Grave, *ACS Catal.* **2018**, 8, 2754.
- [43] Y. Li, Y. Li, X. Xu, C. Ding, N. Chen, H. Ding, A. Lu, *Chem. Geol.* **2019**, 504, 276.
- [44] S. Vempati, J. Mitra, P. Dawson, *Nanoscale Res. Lett.* **2012**, 7, 470.